ACS OMEGA

http://pubs.acs.org/journal/acsodf

Article

Toward the Integration of a Silicon/Graphite Anode-Based Lithium-Ion Battery in Photovoltaic Charging Battery Systems

Niloofar Hamzelui, Li-chung Kin, Julian Köhler, Oleksandr Astakhov, Zhifa Liu, Thomas Kirchartz, Uwe Rau, Gebrekidan Gebresilassie Eshetu,* Tsvetelina Merdzhanova,* and Egbert Figgemeier*

Cite This: *ACS Omega* 2022, 7, 27532−27541

Read Online

ACCESS | Metrics & More | Article Recommendations

ABSTRACT: Solar photovoltaic (PV) energy generation is highly dependent on weather conditions and only applicable when the sun is shining during the daytime, leading to a mismatch between demand and supply. Merging PVs with battery storage is the straightforward route to counteract the intermittent nature of solar generation. Capacity (or energy density), overall efficiency, and stability at elevated temperatures are among key battery performance metrics for an integrated PV−battery system. The performance of high-capacity silicon (Si)/graphite (Gr) anode and $LiNi_{0.6}Mn_{0.2}Co_{0.2}O_2$ (NMC622) cathode cells at room temperature, 45, and 60 °C working temperatures for PV modules are explored. The electrochemical performance of both half and full cells are tested using a specially formulated electrolyte, 1 M $LiPF_6$ in ethylene carbonate: diethyl carbonate, with 5 wt % fluoroethylene carbonate, 2 wt % vinylene carbonate, and 1 wt % (2-cyanoethyl)triethoxysilane. To demonstrate solar charging, perovskite solar cells (PSCs) are coupled to the developed batteries, following the evaluation of each device. An overall efficiency of 8.74% under standard PV test conditions is obtained for the PSC charged lithium-ion battery via the direct-current−direct-current converter, showing the promising applicability of silicon/graphite-based anodes in the PV−battery integrated system.

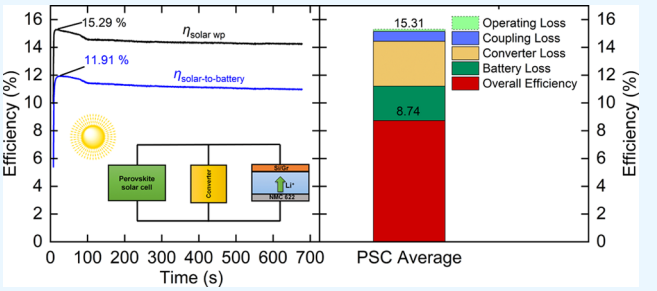

1. INTRODUCTION

Solar photovoltaic (PV) energy generation is highly dependent on weather conditions and only applicable when the sun is shining during the daytime, leading to a mismatch between demand and supply.[1] In this regard, merging PVs with battery storage presents to be the straightforward route to counteract the intermittence of solar generation. The solar cell and batteries can be combined or integrated in a multitude of ways and scales, ranging from indoor applications for "smart houses" and internet of things[2−8] to typical field applications.[9−12] In addition to the power stabilization function, the integration of PV modules with battery storage can potentially minimize the wiring and reduce the need for power management. Properly voltage-matched batteries can serve as a power coupling element and provide the opportunity to avoid maximum power point tracking (MPPT) for PV modules in the directly coupled device.[13,14] To build a PV battery device relevant for outdoor large-scale installations, batteries with potentially low cost and high temperature tolerance are required.[1,15] Particularly, high tolerance to temperatures up to 70 °C is required because high PV energy production, especially in warm climate zones, is associated with module temperatures in the range of 30−60 °C, reaching a maximum up to 70 °C.[16] Ideal batteries to be integrated with the PV module need to have high capacity and a cycle life in the order of 10,000 in the temperature range of −20 to +70 °C using low-cost abundant materials.

Commercial lithium-ion batteries (LIBs) widely use graphite (Gr) as the anode material owing to its high abundance, low cost, high Coulombic efficiency (CE), low working voltage (~0.2 V vs Li/Li^+), and superior cycle life. However, the low theoretical capacity of Gr (372 mA $h{\cdot}g^{-1}$, Li_xC_6, $x \sim 1$) limits its usage in high-energy battery applications. Thus, switching from the Li-ion (Li^+) intercalation (example: graphite) to alloying chemistries (example: silicon) is beneficial to enable high-energy-density batteries. Silicon is one of the most promising alloy-type anode materials with high abundancy, relatively low cost, a low operating voltage (~0.2 to 0.4 V vs Li/Li^+), and high theoretical capacities of 4200 mA $h{\cdot}g^{-1}$ ($Li_{4.4}Si$) and 3590 mA $h{\cdot}g^{-1}$ ($Li_{3.75}Si$) at 415 °C (according to the Li−Si phase diagram[17,18]) and room temperature (RT), respectively. However, despite all the significant features, Si-

Received: May 11, 2022
Accepted: May 20, 2022
Published: July 26, 2022

based anodes present a massive volume change (≥280%) upon lithiation/delithiation, leading to mechanical stress to the anode film, resulting in the pulverization of the Si particles, lower electrical conductivity, an unstable solid−electrolyte interphase (SEI), and lower CCE) than that of graphite.[19,20] To alleviate the challenges associated with both Si and Gr chemistries, the co-utilization of Si and Gr with designer polymeric binders and electrolyte systems via forming a blend or a composite is a rational way as it presents a synergistic advantageous effect of both components.[19,21−24]

The development of high-energy-density rechargeable batteries demands the pairing of high-capacity and/or low-potential anodes with high-capacity and/or high-voltage cathode materials, and therefore, high-capacity and more stable lithium nickel manganese cobalt oxide, NMC622, was deployed as the positive electrode material.[23] Thus, the development of the full cell configuration with a high-capacity Si-based anode and a high-energy lithium nickel manganese cobalt oxide (NMC) cathode could be treated as a promising progress toward next-generation high-energy-density LIBs.[25]

However, much less attention is paid to the performance of the LIB electrolytes at elevated temperatures experienced by solar cells in typical field applications. In our work, we focus on the development of high-capacity Si/Gr anode-based LIB and electrolyte systems with blends of electrolyte additives boosting elevated-temperature operation for the integration with PV devices.

The proof of concept for the solar charging battery system was demonstrated using a lead halide perovskite solar cell (PSC). Perovskite materials have attracted substantial interest for applications such as solar cells[26,27] and light-emitting diodes[28] within the last decade due to their exceptional optoelectronic properties such as low defect densities,[29,30] long recombination lifetimes,[31,32] high absorption coefficients[33] in the visible region, and a band gap that can be adjusted in a relatively wide range.[34,35] Even though PSCs are typically processed from solution and form polycrystalline thin films with a thickness of a few hundred nanometers, they can still achieve power conversion efficiencies of >25%,[36,37] approaching those of much more mature PV technologies such as crystalline silicon. On the lab scale, PSCs provide the possibility to produce high-efficiency small-scale devices for coupling with typical experimental coin cell batteries, which is challenging with usual wafer-based Si PV devices.

In this work, no special voltage matching development has been carried out to realize direct matching of the PSCs and battery cells. Therefore, a direct-current−direct-current (DC−DC) boost converter with MPPT has been applied to realize proper coupling between the PSC and battery following our previous work.[8]

2. EXPERIMENTAL SECTION

2.1. Battery Development. Silicon (Si) alloy (hereafter Si)/graphite (Gr) blend anode films were prepared by using 20 wt % carbon-coated Si alloy (1200 mA h/g) (G7, 3M corp.) and 68 wt % graphite (MagE3, Hitachi, Japan) as active negative electrode (anode) materials, 7.73 wt % sodium carboxymethyl cellulose (CMC) (M_w: 400,000, MTI) and 2.27 wt % lithium poly(acrylic acid) (LiPAA) (PAA, 25 wt % solution in water, M_w = 240,000, Acros, and $LiOH·H_2O$, battery grade, Alfa Aesar) as polymeric binders, and 2 wt % SuperP carbon black (TIMCAL) as an anode electrode conductive additive. The optimized formulation of the anode and slurry preparation steps is described in our previous report.[19] LiPAA and CMC are selected as binders for the Si/Gr blend electrode because of their peculiar features including a high amount of carboxyl groups, no or little swelling while in contact with the electrolyte, high stiffness, and moderate elastomeric properties that can overcome both elastic and plastic deformation during Si volume change. Due to the difference in the chemistry of Si and Gr particles, both binders, which have different affinities to the Si and Gr active materials, are deployed.[38−40] A lithium nickel manganese cobalt oxide (NMC 622) cathode (Custom Cells, Germany) with a loading of 6.4 mg/cm^2 was used as the positive electrode (cathode). The reason why NMC622 is selected for this study, compared to other state-of-the-art cathode materials, such as lithium iron phosphate (LFP) and lithium cobalt oxide (LCO), lies in its well-balanced features—between safety and performance. Despite LFP being the safest with the longest cycle due to its stable chemical makeup, it results in a lower energy density compared to NMC622. LCO, on the other hand, presents to be less structurally stable—being prone to structural change, oxygen release, and thus electrolyte decomposition. The anode was coated on copper (Cu) foil using a coating unit (CUF 5, SUMET, Germany) with four different draw-bar gap thicknesses of 125, 250, 300, and 350 μm, in order to find the optimized negative/positive electrode (N/P) ratio. These electrodes are denoted as Si/Gr-125 μm, Si/Gr-250 μm, Si/Gr-300 μm, and Si/Gr-350 μm, respectively, throughout the manuscript. Electrode thickness, in general, hugely affects the discharge performance, CE, and thus energy efficiency, rate capability, heat generation, temperature distribution, and safety. Thus, an optimum thickness to balance the various performance indicators is needed. 1 M $LiPF_6$ in ethylene carbonate (EC)/diethyl carbonate (DEC) (1:1, w/w) with 5 wt % fluoroethylene carbonate (FEC), 2 wt % vinylene carbonate (VC), and 1 wt % (2-cyanoethyl)triethoxysilane (TEOSCN) was used an electrolyte solution.[41]

Coin cells (2032-type) were assembled in an argon-filled glovebox (O_2 and H_2O < 0.5 ppm) using 90 μL of the electrolyte. The electrochemical performance was measured galvanostatically using Neware BTS4000-5V10mA in the potential window of 0.9−0.01 V versus Li/Li$^+$ for the half cell (anode area of 1.54 cm^2) and 2.5−4.35 V versus Li/Li$^+$ for the full cell (anode and cathode areas of 2.01 and 1.54 cm^2, respectively) configurations. In all experiments, the cells were mounted at an open-circuit potential for 24 h to ensure the electrode wetting prior to being subjected to five formation cycles at 0.05*C*. For long-term measurements, both half and full cells, were measured at 0.2*C*, and for rate capability measurements, *C* rates ranging from 0.05*C* to 3*C* were applied. The half cells and full cells were tested at 45 and 60 °C in order to investigate the effect of elevated temperatures on the performance of the battery. This is because when the battery is paired with a PV, an increase in temperature is expected. The optimized battery was then tested in a PV−battery system at ambient temperature. The optimized full cell was cycled at 0.05*C* for five cycles prior to integration in the PV−battery system, and the capacity of the cell was measured at 0.1*C* after solar charging.

2.2. Solar Cell Development. PSCs were fabricated in-house using the following procedure: indium tin oxide (ITO) substrates (2.0 × 2.0 cm^2, Yingkou Youxuan Trade Co.,Ltd.) were cleaned with soap, deionized (DI) water, acetone, and isopropanol (IPA) in an ultrasonic bath in succession for 10

https://doi.org/10.1021/acsomega.2c02940
ACS Omega 2022, 7, 27532−27541

min each. Afterward, the substrates were treated with oxygen plasma for 12 min and transferred to a nitrogen (N_2)-filled glovebox. Then, 80 μL of poly(triaryl) amine (PTAA, 2.0 mg/mL in toluene) at 75 °C was spin-coated on the substrates using a two-step program of 500 rpm for 4 s and then 4500 rpm for 20 s. The layer was subsequently annealed at 110 °C for 10 min and cooled back down to RT. Subsequently, 120 μL of perovskite precursor solution consisting of lead(II) acetate [Pb $(CH_3COO)_2{\cdot}3H_2O$, 0.54 M], lead chloride ($PbCl_2$, 0.06 M), dimethyl sulfoxide (0.6 M), and methylammonium iodide (1.8 M) in dimethylformamide was spin-coated on the top of the PTAA layer in another two-step process, consisting of 10 s of 900 rpm, followed by 30 s at 6000 rpm. Immediately after, the samples were annealed at 75 °C for 2 min and cooled down to RT. On the top of the perovskite layer, 65 μL of phenyl-C_{61}-butyric acid methyl ester (20 mg/mL) at 75 °C was spin-coated at 1200 rpm for 60 s and then dried in air, forming the electron transport layer. To finalize the coating process, 100 μL of bathocuproine (0.5 mg/mL in IPA) was spin-coated on the top at 4000 rpm for 30 s. As the final step of solar cell fabrication, silver contacts were evaporated in a separate vacuum chamber through a shadow mask to define the final cell area of 1.08 cm^2, where silver and ITO overlap. For more details on this general type of PSC, please refer to refs 31 and 42−44 that include various additional characterization results. The solar cell was then characterized under standard test conditions by using a sun simulator Wacom solar simulator WXS-140S-Super.

2.3. DC−DC Booster Converter. The SPV 1040-TSSOP8 step-up voltage converter from STMicroelectronics was selected for its maximum power point (MPP) tracker algorithm as well as its stable working and output voltage characteristics. Converter performance is described by conversion efficiency

$$\eta_{\text{conversion}} = \frac{P_{\text{out}}}{P_{\text{in}}} \times 100\% \tag{1}$$

and the coupling factor

$$\text{coupling factor} = \frac{P_{\text{in}}}{P_{\text{mpp}}} \tag{2}$$

where P_{in} is the power delivered from the solar cell to the converter, P_{out} is the power delivered to the battery from the converter, and P_{mpp} refers to the solar cell MPP. The coupling factor reveals how close the working of the solar cell is to the MPP. The converter efficiency represents the fraction of energy transferred by the converter.

2.4. Operation of the PV−Battery System. Following the characterization of both the battery and solar cells as separate units, tests on the coupled devices were carried out. The batteries were set into an in-house-built holder connected to the solar cells and then charged by the solar cells illuminated using the solar simulator. The circuit diagram for the computer-controlled measurement system is shown in Scheme 1.

The charging experiments were conducted using an SPV 1040-TSSOP8 step-up voltage converter from STMicroelectronics to boost the incoming voltage from the solar cell to a level that allows charging of the battery.

The performance of the PV−battery integrated system is defined by the solar charging efficiency, $\eta_{\text{solar-to-batt}}$

Scheme 1. Circuit Diagram of the Measurement Setup with the Solar Cell, Converter, and Battery as Main Components

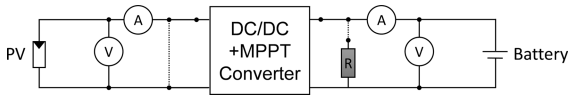

$$\eta_{\text{solar-to-batt}} = \frac{V_c I_c}{A \times P_{\text{AM1.5}}} \times 100\% \tag{3}$$

and battery round trip efficiency, $\eta_{\text{round-trip}}$

$$\eta_{\text{round-trip}} = \frac{\int_0^{\text{td}} P_d \, dt}{\int_0^{\text{tc}} P_{\text{out}} \, dt} \times 100\% \tag{4}$$

and the overall system efficiency (η_{overall}) is given by

$$\eta_{\text{overall}} = \eta_{\text{solar-to-batt}} \times \eta_{\text{round-trip}} \tag{5}$$

where V_c and I_c refer to the charging voltage and current of the battery, respectively, $P_{\text{AM1.5}}$ is the incident light power density under AM1.5 conditions (100 mW cm^{-2}), and A is the effective area of the PSC. P_{out} and P_d are the instantaneous charging and discharging powers of the battery, respectively. Solar charging efficiency measures how efficiently the input power of light is delivered to the battery, including the voltage step-up losses and power overheads from the converter. Battery round trip efficiency is the fraction of energy stored in the battery that can be extracted from the immediately preceding charge cycle. It is defined as the integral of the battery power during discharge (P_d) with respect to the discharge time (t_d) over the integral of the battery power during charging (P_{out}) with respect to the charging time (t_c). The charging time t_c is set to 700 s in our experiment. The discharge time t_d is defined as the time between the moment when the discharge started and the moment when the battery voltage reaches 2.5 V, which is the initial voltage for the charge phase. The overall efficiency is the product of the solar charging efficiency and the battery round trip efficiency.

3. RESULTS AND DISCUSSION

3.1. Battery Development. *3.1.1. Optimization of the Si/Gr Anode for a Full Cell Configuration.* To design an optimized full cell battery, the capacity of the Si/Gr anode with respect to that of the NMC622 cathode, that is, the ratio of the capacity of the negative to positive electrode (N/P), needs to be balanced. In this work, NMC622 with a fixed areal capacity of 1.155 mA h·cm^{-2} was used; therefore, the N/P ratio was balanced by adjusting the anode thickness (active mass balance). The N/P ratio is a crucial parameter as it influences the long-term performance, energy density, safety, and battery costs in the full cell format. Lithium plating is one of the problems that can occur due to an unbalanced N/P ratio, leading to irreversible capacity loss. At N/P ratios <1, there are not enough sites on the anode to accommodate all the Li^+ coming from the cathode, which can result in lithium plating during long-term cycling.[45,46] Therefore, for safety reasons and improving the cycle life of the battery, a slightly higher capacity of the anode is needed. Large oversizing of the anode increases the mass and volume that is not used (inactive mass)[47] and thus decreases the specific energy. For this reason, anode films of different thicknesses were prepared with 125, 250, 300, and 350 μm draw-bar gaps. It is necessary to have a balance

https://doi.org/10.1021/acsomega.2c02940
ACS Omega 2022, 7, 27532−27541

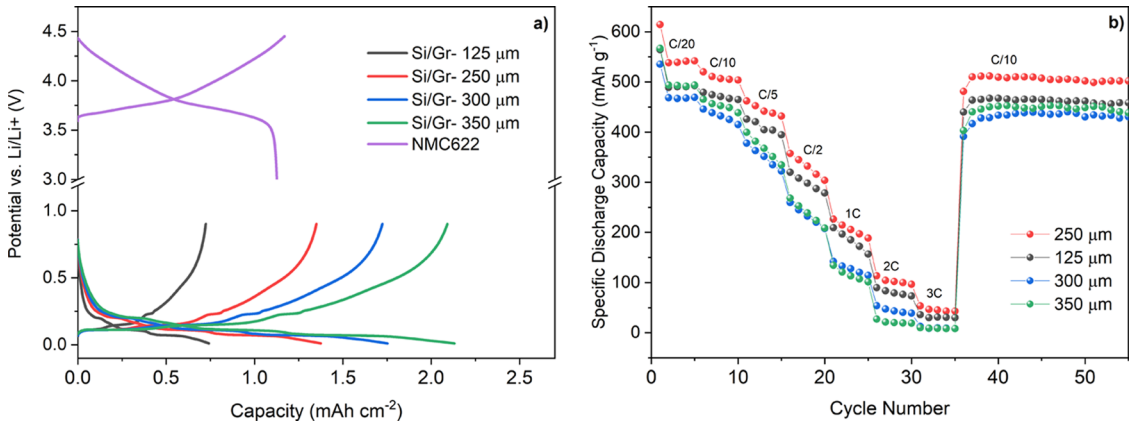

Figure 1. (a) Charge−discharge profile at the second cycle for the NMC622 cathode half cell and Si/Gr anode half cells with different anode thicknesses, (b) rate capability at 0.05*C*, 0.1*C*, 0.2*C*, 0.5*C*, 1*C*, 2*C*, and 3*C* for Si/Gr anode half cells with different anode thicknesses.

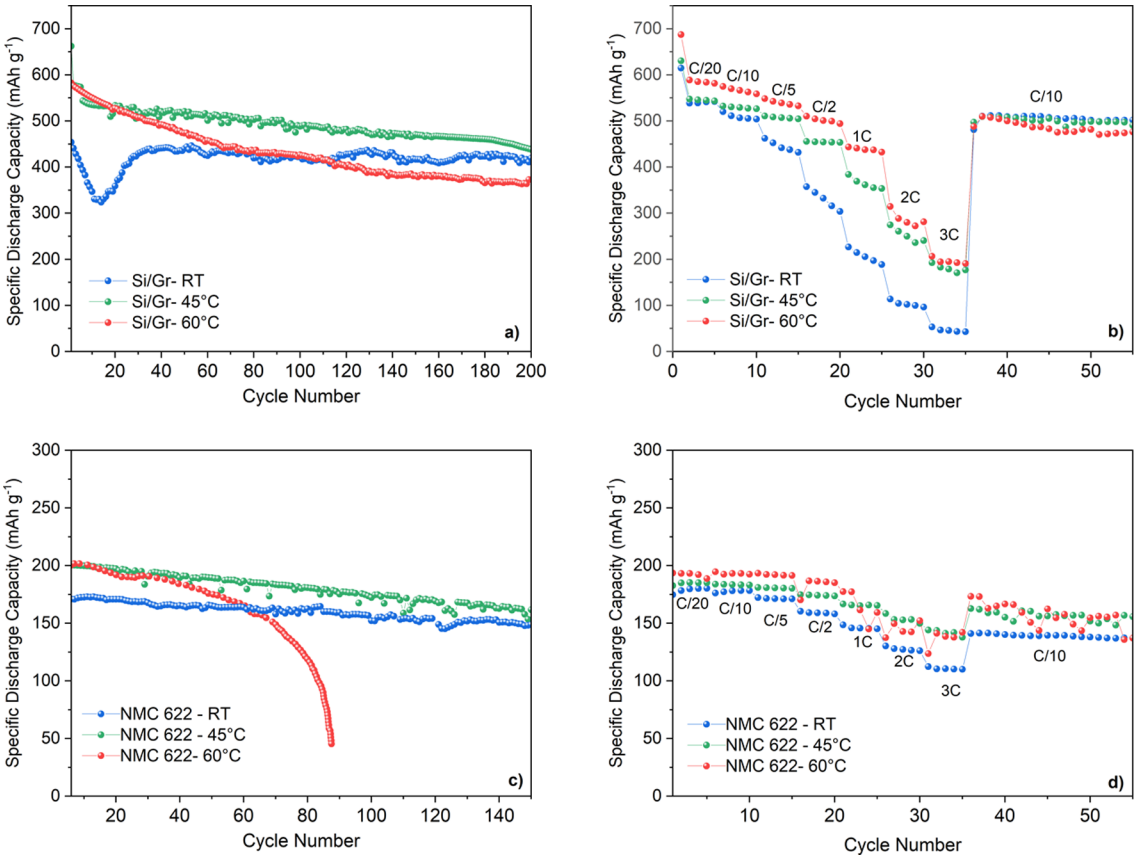

Figure 2. (a) Cycling performance at 0.2*C*, (b) rate capability at 0.05*C*, 0.1*C*, 0.2*C*, 0.5*C*, 1*C*, 2*C*, and 3*C* for Si/Gr anode half cells at RT, 45, and 60 °C, (c) cycling performance at 0.2*C*, and (d) rate capability at 0.05*C*, 0.1*C*, 0.2*C*, 0.5*C*, 1*C*, 2*C*, and 3*C* for NMC622 cathode half cells RT, 45, and 60 °C.

between the safety and ideal specific capacity, which are gained by $Q_{Anode}/Q_{Cathode} > 1$ and $Q_{Anode}/Q_{Cathode} = 1$, respectively, and is found to be between 1.1 and 1.2.[48]

Figure 1a shows the charge−discharge profile for anode half cells built from the Si/Gr blended anode of different thicknesses as well as cathode half cells at the second cycle at 0.05C. The plot depicts that Si/Gr-125 μm shows an N/P ratio of 0.63, which is lower than 1. Si/Gr-250 μm has an N/P ratio of 1.18. However, for anodes coated with 300 and 350 μm draw-bar gaps, the N/P ratios are 1.36 and 1.81, respectively, which are considered too high to be applied. Therefore, Si/Gr-250 μm (1.365 mA h·cm^{-2}, active mass loading of 2.6 mg cm^{-2}) was chosen as the optimized anode thickness for the construction of full battery cells. Figure 1b shows the specific discharge capacity (in milliampere hours per gram) versus cycle number of Si/Gr blended anode half cells with different thicknesses at different *C* rates, ranging from 0.05C to 3C. After cycling at 3C, the cells were cycled at 0.1C to investigate the capacity recovery after fast charging/discharging. At all *C* rates, Si/Gr-250 presented the highest capacity compared to the other anodes and shows a high capacity recovery of 98.36% after being subjected to fast

https://doi.org/10.1021/acsomega.2c02940
ACS Omega 2022, 7, 27532−27541

cycling (at 3C). Si/Gr-125, Si/Gr-300, and Si/Gr-350 show capacity recoveries of 97.47, 97.31, and 97.25%, respectively. For all the above-mentioned reasons, Si/Gr-250 was chosen as the optimized anode thickness and was utilized in the subsequent measurements.

3.1.2. Effect of Temperature on the Electrochemical Performance of the Battery. Solar cells operate mostly at elevated temperatures, and thus, LIBs operating in a PV−battery system need to have a suitable performance not only at RT but also at elevated temperatures. According to the Arrhenius law (eq 6), the chemical reaction rate is directly correlated with the temperature, implying that an increase in temperature results in an exponential rise in electrochemical reaction rates.

$$k = A \exp\left(\frac{-E_a}{RT}\right) \tag{6}$$

where R, T, E_a, and A are the gas constant, absolute temperature, energy of action, and prefactor, respectively.

For this reason, the performance of Si/Gr||NMC622 cells was investigated at RT, 45, and 60 °C. For a deeper understanding of the charge/discharge mechanism at elevated temperatures, Si/Gr and NMC622 half cells (vs Li/Li^+) were investigated separately at the above-mentioned temperatures.

Figure 2a presents the cycling performance of Si/Gr anode half cells at 0.2C at the three different temperatures. At elevated temperatures, the Si/Gr half cells initially showed higher capacities than that at RT. The obtained initial capacities are 454.05, 544.04, and 582.31 mA h g^{-1} at RT, 45, and 60 °C respectively. However, the rate of capacity loss at 45 and 60 °C is higher than that at RT. After 200 cycles, the capacity retention values of the anode half cells at RT, 45, and 60 °C are 92.41, 79.24, and 62.46%, respectively. The decrease in capacity upon cycling with increasing temperature could be explained by the fact that parasitic reactions including electrolyte decomposition, evolution of active oxygen from the NMC cathode, and so forth are aggravated at elevated temperatures. This could be further accelerated by the higher Li^+ mobility at higher temperatures. Therefore, initially, because the charge/discharge mechanism is controlled by diffusion, the capacity is higher at elevated temperatures.[49] It has been reported that TEOSCN as an additive improves the electrochemical performance at higher temperatures compared to that at lower temperatures.[41] It is reported that the SEI layer in a system with 1 M $LiPF_6$ EC/DEC (1:1) breaks down at about 57 °C, providing more access to fresh reactive active materials for the electrolyte constituents (solvent molecules, salt, and additives) and thus leading to lower electrochemical performance of the cell at elevated temperatures.[50] $LiPF_6$ breaks down at elevated temperatures (eq 7), leading to the formation of highly reactive species, such as PF_5. In the presence of unavoidable traces of moisture in the cell, PF_5 reacts with water, leading to the formation of POF_3 and HF (eq 8). PF_5 also reacts with EC and DEC solvents. Scheme 2 shows the possible mechanism for the EC decomposition via a strong Lewis acid, PF_5.[51]

$$LiPF_6(s) \leftrightarrow LiF(s) + PF_5(g) \tag{7}$$

$$PF_5(g) + H_2O(l) \rightarrow POF_3(g) + 2HF(l) \tag{8}$$

Hence, considering all the facts mentioned, elevated temperatures are initially favorable, as evidenced by the higher capacities. However, during long-term cycling, the capacity

Scheme 2. Possible Mechanism for the EC Decomposition via a Strong Lewis Acid, PF_5

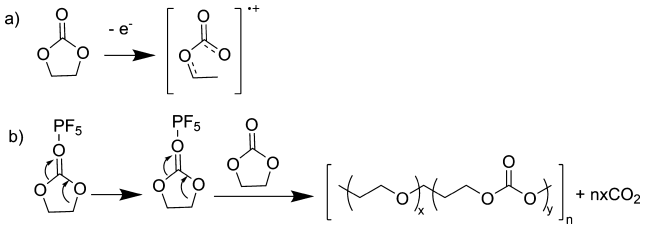

rapidly drops compared to that of the cells cycled at RT. This could be linked to the generation of high current, causing an enhanced heat dissipation [according to RI^2 (R = resistance and I = current)] and resulting in higher internal temperature and thus accelerated cell degradation.

Figure 2b shows the rate capability of Si/Gr anode half cells at RT, 45, and 60 °C. The C rate ranges from 0.05C to 3C, and afterward, the cells were cycled at 0.1C to measure the capacity recovery of the cells, which are found to be 98.36, 95.74, and 88.65% at RT, 45, and 60 °C respectively. It is observed that at higher C rates, cells cycled at elevated temperatures show higher capacities, which is most likely due to the enhanced Li^+ diffusion at elevated temperatures. Figure 2c depicts the cycling performance of the NMC622 cathode versus Li/Li^+ at RT, 45, and 60 °C. NMC622 cathode half cells demonstrated the same trend as that of Si/Gr half cells (Figure 2a). However, at 60 °C, it is observed that the rapid capacity loss and decrease in CE for NMC622 half cells starts at ∼70 cycles (74.34% capacity retention), which is much faster compared to that of the Si/Gr half cells. The capacity retention values of NMC622 half cells cycled at RT and 45 °C at the 150th cycle are 86.96 and 80.66%, respectively. Increasing the temperature reduces the cyclability of the NMC 622 cathode due to challenges such as accelerated metal dissolution, active oxygen evolution and thus reaction with the electrolyte solvents, and cation mixing since the ionic radius of Li^+ and Ni^{2+} are similar.[52,53] 60 °C is a typical temperature where $LiPF_6$ significantly decomposes, resulting in highly acidic species such as PF_5, HF, and POF_3 (Scheme 2). These species in turn catalyze the cathode-related reactions, causing fast degradation in capacity. Direct reactions of the acidic species with the NMC cathode at higher temperature causes transition metal cation dissolution, oxygen evolution and thus electrolyte oxidation, and structural disorder. When TEOSCN is added as an electrolyte additive, it leads to the formation of (1) a robust cathode−electrolyte interphase and (2) a layer of physical barrier of the −C≡N−TM complex (TM = transition metal), both effectively inhibiting the direct reaction between the NMC active material and $LiPF_6$-derived acidic species.[41] Figure 2d depicts the rate capability measurements of NMC622 half cells at RT, 45, and 60 °C. The capacity at elevated temperatures is higher; however, compared to the rate capability of Si/Gr anode half cells (Figure 2b), the difference in capacity at the different temperatures is much lower. Capacity recoveries after cycling at 3C are found to be 80.24, 88.17, and 88.92% at RT, 45, and 60 °C, respectively.

Figure 3a presents the differential capacity (dQ/dV) versus potential (V) for the Si/Gr|NMC622 full cells at RT, 45, and 60 °C. To better understand the electrochemical and degradation phenomena, dQ/dV analysis was performed at a low C rate (0.05C). It is observed that by increasing the

https://doi.org/10.1021/acsomega.2c02940
ACS Omega 2022, 7, 27532−27541

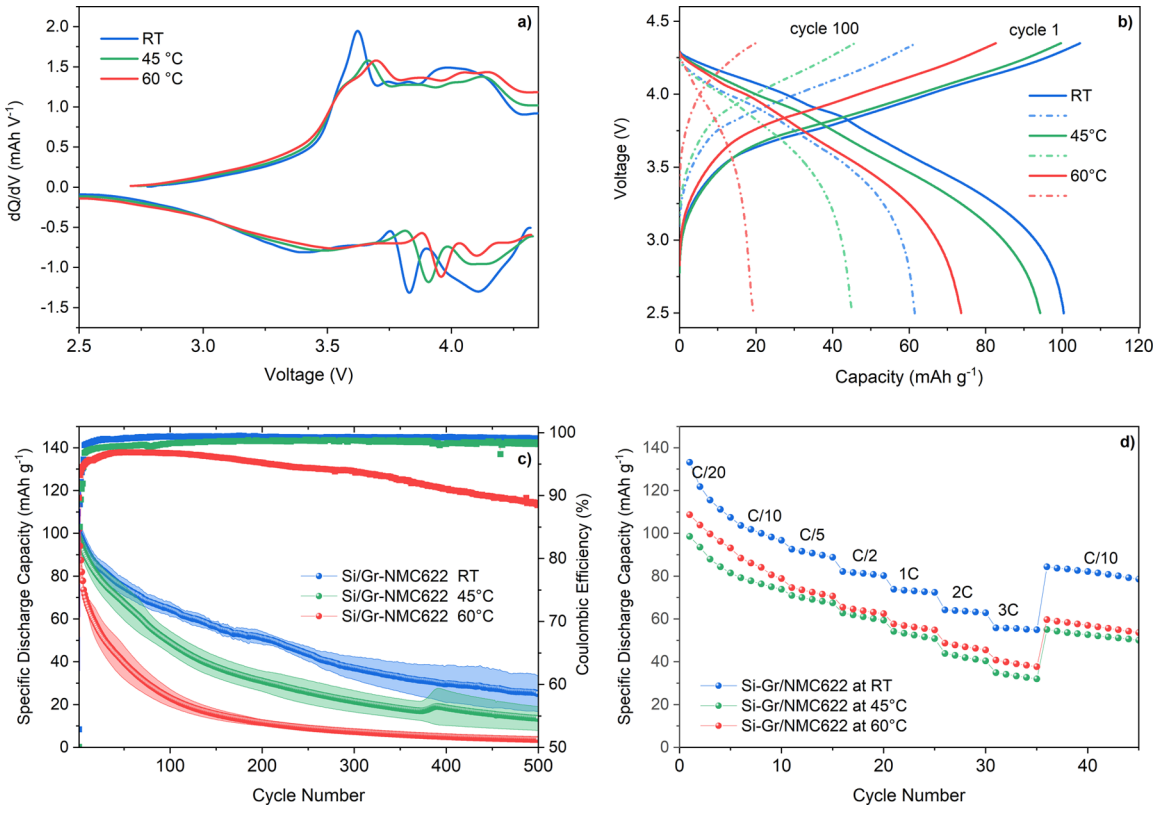

Figure 3. (a) Differential capacity (dQ/dV) vs voltage at the second cycle at 0.05C, (b) charge−discharge profile at 0.2C, (c) cycling performance and CE at 0.2C, and (d) rate capability at 0.05C, 0.1C, 0.2C, 0.5C, 1C, 2C, and 3C, for Si/Gr||NMC622 full cells at RT, 45, and 60 °C.

temperature, the intensity of the charge/discharge peaks is decreased, and the peaks become narrower and are shifted to higher voltages. Figure 3b shows a typical charge−discharge profile of the full cells cycled using a galvanostatic testing protocol, evidencing lower capacity retention at elevated temperatures. Figure 3c portrays the long-term cycling performance of the full cells at RT, 45, and 60 °C. The capacity retention values of the cells at the second cycle are 98.78, 98.71, and 97.23% at RT, 45, and 60 °C, respectively. These values are reduced to 74.23, 69.25, and 50.31% in the 50th cycle, respectively. The CEs at the second cycle for the cells cycled at RT, 45, and 60 °C are 97.99, 96.76, and 93.22%, respectively. In the 50th cycle, the CE values are 99.11% at RT, 97.85% at 45 °C, and 96.85% at 60 °C. Though the values are significantly high, the CEs obtained in this study are opted to be improved via further optimization of the electrolyte composition and the electrode−electrolyte interphases. Figure 3d shows the rate capability tests of the full cells at three different temperatures. These results are in agreement with the results from Figure 3c, showing higher capacities at RT than at 45 and 60 °C. The capacity recovery values after the cells are subjected to cycling at a higher rate (ca. 3C) are 81.43, 69.44, and 67.55% at RT, 45, and 60 °C, respectively.

In full cells, due to the limited amount of Li^+ present in the cell, the electrochemical performance is restricted by the kinetics of Li^+ insertion/extraction and diffusion through the SEI and cathode electrolyte interphase (CEI) layers.[19] Therefore, despite the initial high capacity in Si/Gr|Li and NMC622|Li half cells at 45 and 60 °C, which is due to the increase in the diffusion of unlimited Li^+, Si/Gr||NMC622 full cells show higher initial capacity and a lower rate of capacity loss at RT than at elevated temperatures.

3.2. PV−Battery Integrated System. The newly developed battery has been tested together with the PSC to validate its solar charging ability. The DC−DC boost converter ensures that the MPP of the cell is tracked over time. Figure 4 shows the I−V characteristics of the PSC measured in forward and reverse directions. The cell had an open-circuit voltage of 1.25 V and a short-circuit current density of 15.9 mA/cm^2. The fill factor is found to be 77.0%, resulting in an efficiency of 15.31%. The MPP is marked with a blue star, and positions of

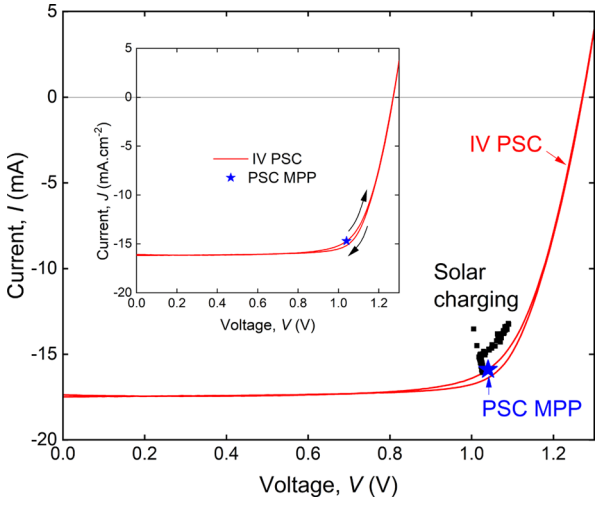

Figure 4. Current−voltage (I−V) curve of the PSC with the MPP (blue) and solar charging working points (black). The inset shows the IV characteristic of the PSC with indicated short-current density J_{sc} values.

https://doi.org/10.1021/acsomega.2c02940
ACS Omega 2022, 7, 27532−27541

the working point during charging are shown with black rectangles. The MPP tracker in most cases succeeded to maintain a working point in the vicinity of the MPP during charging. The working point variation is complex and is a result of both the operation of the MPPT and the increase in the state of charge of the battery. It can be seen from the working points of the coupled system superimposed as black squares that they begin close to the MPP, then drift back for the majority of the operation, and finally trace out a parallel IV curve. The latter effect is due to the battery voltage reaching the safety voltage, causing the MPPT to stop working and enter a fixed current mode. Note that the offset between the solar cell $I-V$ characteristics and the working points is related to the difference in the measurement procedure as well. While reference IV measurements are performed using the standard four-point probe method excluding the effect of wire resistance, the wiring resistive losses are inevitably present in the charging experiment. The total voltage drop in all wire connections results in the shift of the working points to lower voltages.

In Figure 5, the charge−discharge cycle of the solar-charged battery is shown with black lines for the voltage and red lines

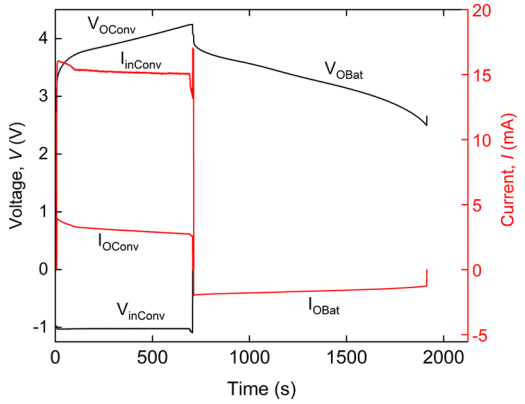

Figure 5. Charge and discharge voltages (black), currents (red) during PSC charge and battery discharge, where 700 s is the charging time and 1200 s is the discharge time.

for the current. The incoming voltage of approximately 1 V supplied by the solar cell (shown negative for clarity) is boosted by the converter to the battery relevant range of approximately 4 V. The voltage is drifting from approximately 3.5 V in the beginning of the charge period to the final value of 4.24 V after 700 s, presumably following the increase in battery voltage during charge. At the same time, the current delivered to the converter from the solar cell (I_{inConv}) is reduced, inversely proportional to the voltage boost. After the charging phase was over, a battery open-circuit voltage (V_{OBat}) of 4.09 V has been observed. At the beginning of the discharge phase, the battery voltage was 3.93 V, and it declined to 2.5 V over 1200 s of discharge. In Figure 5, it can be seen that the input current reduces at two very distinct rates, initially very quickly and then stabilizing. This is likely due to the converter stepping up the voltage instead of the degradation of the solar cell. The initial sharp decrease in the input converter current (I_{inConv}) corresponds to the logarithmic increase of the voltage output of the converter. Converter output voltage then enters a quasi-linear upward trend as the battery charges to higher voltages at a steady rate, and the converter input current stabilizes accordingly. This almost abrupt change in current is due to the MPPT holding input voltage of the converter at an almost constant voltage. Thus, output power variations and increases in impedance from higher voltage boosts will reflect fully in the input current, resulting in what looks like a drift in the working point resembling a degrading solar cell. This offset is what is described as "converter losses" in the loss analysis in the later session.

The coupling factor and converter efficiency during the charge phase are presented in Figure 6. The coupling factor

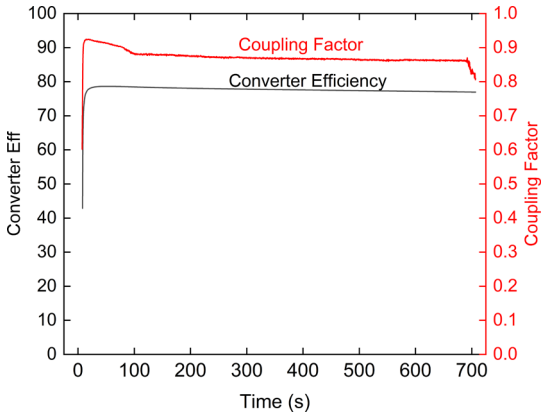

Figure 6. Coupling factor and converter efficiency over a charging time of 700 s.

essentially describes the quality of the MPPT where 100% represents ideal tracking—the situation when the working point coincides with the MPP of the solar cell. It is common for high-quality MPPT devices to provide coupling or tracking efficiency very close to 100%.[54,55] In this study, the coupling factor peaked at 92.4% in the beginning and declined to 87.3% at the end of the charge phase. The decrease could be due to the increased voltage step up, in which more power is needed to convert current into voltage. Due to the relatively low input voltage of 1 V, the decline of 5% in the coupling factor is close to the expected performance of this converter. Average power conversion efficiency of the DC−DC converter was 77.7% across the charging phase. The converter efficiency did not change during the whole charging cycle, indicating that the input power was constant.

The energy loss analysis of the solar charging process was performed to compare where the losses were attributed to. From Figure 7, average efficiencies are plotted on the right bar chart, while efficiency of the solar cell and the overall solar-to-battery efficiency are plotted on the left. When compared to the efficiency of the solar cell, as determined from the $I-V$ curve (15.31%), the operating losses are initially minimal but

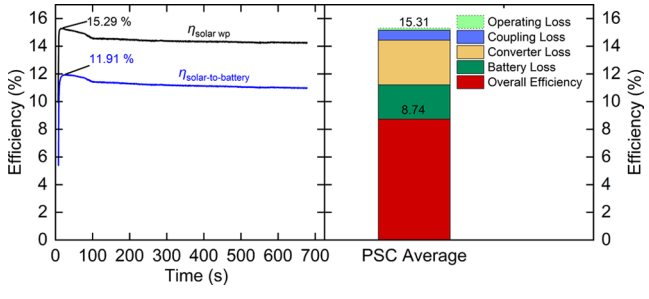

Figure 7. Energy loss analysis of the solar charging process.

https://doi.org/10.1021/acsomega.2c02940
ACS Omega 2022, 7, 27532−27541

expand after the first 60 s. The coupling losses initially track this closely but slowly increase as the battery charges up.

Overall, losses are mainly originating from the converter (beige region in Figure 7) with the next highest losses being associated with the battery (an absolute loss of 2.47% efficiency), which has a measured average battery roundtrip efficiency of 77.97%. It should be noted that compared to the battery-associated losses in previously published results, 8, these losses are relatively lower. This results in a final overall efficiency of 8.74%, considering the initial PSC efficiency of 15.31%. Given that the effective *C* rates of 2.06 in this experiment are relatively high, the fact that such a high efficiency is achieved is notable and a testament to the success of our developed battery.

4. CONCLUSIONS

In summary, lithium-ion battery (LIB) built based on a blended silicon (Si)/graphite (Gr) anode and an NMC622 cathode with an electrolyte containing high-temperature enabler additive was developed to withstand the high temperature and *C* rate required for integrated solar battery charging. The optimized battery was utilized with a solar cell of similar size using a booster converter to validate the results with a real charging current profile. Such an innovation is essential for safe and long-term usage of LIBs under conditions that could easily lead to thermal runaway.

Aiming at optimizing the individual battery compartments, tests were conducted on Si/Gr|Li and NMC622|Li cells separately in an electrolyte involving a high-temperature enabler TEOSCN-based additive. The individual half cells and full cells were tested at RT and elevated temperatures of 45 and 60 °C and at high *C* rates up to 3C. Both anode and cathode half cells show higher initial capacities at elevated temperatures, followed by rapid capacity loss. Especially the cathode showed extreme capacity loss after almost 60 cycles. The Si/Gr||NMC622 cells have a similar trend in the initial capacities at RT and elevated temperature. At 60 °C, the battery showed fast capacity loss similar to the cathode half cells, which suggests that further development efforts have to be directed toward stabilizing the cathode capacity and preventing rapid capacity loss at elevated temperature by further optimizing the formulation of electrolyte additives. After deep charge/discharge at 3C, the Si/Gr anodes showed capacity recovery values of 98.36 and 88.65% at RT and 60 °C, respectively. In general, the low-cost and environmentally friendly TEOSCN-based additive in combination with Si/Gr anode-based LIBs proved to be suitable for high-temperature application of the PV−battery system.

The developed LIB was effectively paired with a 15.31% efficient PSC, by using a DC−DC boost MPPT converter, resulting in a respectable 8.74% overall efficiency under 2C charge rates at RT.

This experiment is further evidence that high-capacity Si-based anodes in combination with an electrolyte containing TEOSCN as an additive are promising directions for the development of compact PV−battery integrated systems. The increased temperatures experienced during solar charging at peak rates correlate well with the increased anode performance at higher temperatures. With a better choice of the cathode or further optimization of the Si-based anode blend to unlock the full potential of silicon, such a high-temperature performance electrolyte will be useful to ensure safe and environmentally friendly development of integrated solar battery systems.

AUTHOR INFORMATION

Corresponding Authors

Gebrekidan Gebresilassie Eshetu − *Aging Processes and Lifetime Prediction of Batteries, Institute for Power Electronics and Electrical Drives (ISEA), RWTH Aachen University, 52066 Aachen, Germany; Department of Chemistry, College of Natural and Computational Sciences, Mekelle University, 231 Mekelle, Ethiopia;* orcid.org/0000-0001-8834-2766; Email: gebrekidan.eshetu@isea.rwth-aachen.de

Tsvetelina Merdzhanova − *IEK-5 Photovoltaics, Forschungszentrum Jülich GmbH, 52425 Jülich, Germany;* Email: t.merdzhanova@fz-juelich.de

Egbert Figgemeier − *Aging Processes and Lifetime Prediction of Batteries, Institute for Power Electronics and Electrical Drives (ISEA), RWTH Aachen University, 52066 Aachen, Germany; Helmholtz-Institute Münster (HI MS): Ionics in Energy Storage (IEK-12), Institute of Energy and Climate Research, Forschungszentrum Jülich GmbH, 48149 Münster, Germany;* Email: e.figgemeier@fz-juelich.de

Authors

Niloofar Hamzelui − *Aging Processes and Lifetime Prediction of Batteries, Institute for Power Electronics and Electrical Drives (ISEA), RWTH Aachen University, 52066 Aachen, Germany*

Li-chung Kin − *IEK-5 Photovoltaics, Forschungszentrum Jülich GmbH, 52425 Jülich, Germany;* orcid.org/0000-0002-7936-9585

Julian Köhler − *Aging Processes and Lifetime Prediction of Batteries, Institute for Power Electronics and Electrical Drives (ISEA), RWTH Aachen University, 52066 Aachen, Germany; IEK-5 Photovoltaics, Forschungszentrum Jülich GmbH, 52425 Jülich, Germany*

Oleksandr Astakhov − *IEK-5 Photovoltaics, Forschungszentrum Jülich GmbH, 52425 Jülich, Germany;* orcid.org/0000-0001-8499-058X

Zhifa Liu − *IEK-5 Photovoltaics, Forschungszentrum Jülich GmbH, 52425 Jülich, Germany;* orcid.org/0000-0003-1068-4867

Thomas Kirchartz − *IEK-5 Photovoltaics, Forschungszentrum Jülich GmbH, 52425 Jülich, Germany;* orcid.org/0000-0002-6954-8213

Uwe Rau − *IEK-5 Photovoltaics, Forschungszentrum Jülich GmbH, 52425 Jülich, Germany*

Complete contact information is available at: https://pubs.acs.org/10.1021/acsomega.2c02940

Author Contributions

N.H.: conceptualization, investigation, writing—original draft, and writing—review and editing. L.K.: conceptualization, investigation, writing—original draft, and writing—review and editing. J.K.: investigation. Z.L.: resources and writing—review and editing. T.K.: writing—review and editing. U.R.: supervision. O.A.: conceptualization, writing—original draft, writing—review and editing, and supervision. G.G.E.: conceptualization, writing—original draft, writing—review and editing, and supervision. T.M.: conceptualization, supervision, writing—original draft, and writing—review and editing. E.F.: conceptualization and supervision.

Notes

The authors declare no competing financial interest.

https://doi.org/10.1021/acsomega.2c02940
ACS Omega 2022, 7, 27532−27541

■ ACKNOWLEDGMENTS

N.H. and E.F. acknowledge project "GrEEn" (no. 313-W044B), which is supported by the Ministry for Economy, Innovation, Digitalization and Energy of the state NRW. G.G.E. and E.F. acknowledge the funding received from the European Commission via the H2020 IMAGE project (grant agreement no: 769929—IMAGE—H2020-GV-2016-2017/H2020-GV-2017). Z.L. and T.K. acknowledge the Helmholtz Association for the project PEROSEED.

■ REFERENCES

(1) Vega-Garita, V.; Ramirez-Elizondo, L.; Narayan, N.; Bauer, P. Integrating a Photovoltaic Storage System in One Device: A Critical Review. *Prog. Photovoltaics Res. Appl.* **2019**, *27*, 346−370.
(2) Alippi, C.; Camplani, R.; Galperti, C.; Roveri, M. A Robust, Adaptive, Solar-Powered WSN Framework for Aquatic Environmental Monitoring. *IEEE Sens. J.* **2011**, *11*, 45−55.
(3) Belu, R. R. Design and Analysis of a Micro-Solar Power for Wireless Sensor Networks. *2012 9th International Conference on Communications*, 2012; pp 275−278.
(4) Bogue, R. Solar-Powered Sensors: A Review of Products and Applications. *Sens. Rev.* **2012**, *32*, 95−100.
(5) Agbo, S. N.; Merdzhanova, T.; Yu, S.; Tempel, H.; Kungl, H.; Eichel, R.-A.; Rau, U.; Astakhov, O. Photoelectrochemical Application of Thin-Film Silicon Triple-Junction Solar Cell in Batteries. *Phys. Status Solidi A* **2016**, *213*, 1926−1931.
(6) Agbo, S. N.; Merdzhanova, T.; Yu, S.; Tempel, H.; Kungl, H.; Eichel, R.-A.; Rau, U.; Astakhov, O. Development towards Cell-to-Cell Monolithic Integration of a Thin-Film Solar Cell and Lithium-Ion Accumulator. *J. Power Sources* **2016**, *327*, 340−344.
(7) Sandbaumhüter, F.; Agbo, S. N.; Tsai, C. L.; Astakhov, O.; Uhlenbruck, S.; Rau, U.; Merdzhanova, T. Compatibility Study towards Monolithic Self-Charging Power Unit Based on All-Solid Thin-Film Solar Module and Battery. *J. Power Sources* **2017**, *365*, 303−307.
(8) Kin, L.-c.; Liu, Z.; Astakhov, O.; Agbo, S. N.; Tempel, H.; Yu, S.; Kungl, H.; Eichel, R.-A.; Rau, U.; Kirchartz, T.; Merdzhanova, T. Efficient Area Matched Converter Aided Solar Charging of Lithium Ion Batteries Using High Voltage Perovskite Solar Cells. *ACS Appl. Energy Mater.* **2020**, *3*, 431−439.
(9) Weniger, J.; Tjaden, T.; Quaschning, V. Sizing of Residential PV Battery Systems. *Energy Proc.* **2014**, *46*, 78−87.
(10) Merei, G.; Moshövel, J.; Magnor, D.; Sauer, D. U. Optimization of Self-Consumption and Techno-Economic Analysis of PV-Battery Systems in Commercial Applications. *Appl. Energy* **2016**, *168*, 171−178.
(11) Li, W.; Kerr, E.; Goulet, M. A.; Fu, H. C.; Zhao, Y.; Yang, Y.; Veyssal, A.; He, J. H.; Gordon, R. G.; Aziz, M. J.; Jin, S. A Long Lifetime Aqueous Organic Solar Flow Battery. *Adv. Energy Mater.* **2019**, *9*, 1900918.
(12) Millet, L.; Berrueta, A.; Bruch, M.; Reiners, N.; Vetter, M. Extensive Analysis of Photovoltaic Battery Self-Consumption: Evaluation through an Innovative District Case-Study. *Appl. Phys. Rev.* **2019**, *6*, 021301.
(13) Paul Ayeng'o, S.; Axelsen, H.; Haberschusz, D.; Sauer, D. U. A Model for Direct-Coupled PV Systems with Batteries Depending on Solar Radiation, Temperature and Number of Serial Connected PV Cells. *Sol. Energy* **2019**, *183*, 120−131.
(14) Astakhov, O.; Merdzhanova, T.; Kin, L.-C.; Rau, U. From Room to Roof: How Feasible Is Direct Coupling of Solar-Battery Power Unit under Variable Irradiance? *Sol. Energy* **2020**, *206*, 732−740.
(15) Gurung, A.; Qiao, Q. Solar Charging Batteries: Advances, Challenges, and Opportunities. *Joule* **2018**, *2*, 1217−1230.
(16) Dupré, O.; Vaillon, R.; Green, M. A. *Thermal Behavior of Photovoltaic Devices*; SpringerLink, 2017.
(17) Boukamp, B. A.; Lesh, G. C.; Huggins, R. A.; Soc, J. E. All-Solid Lithium Electrodes with Mixed-Conductor Matrix. *J. Electrochem. Soc.* **1981**, *128*, 725−729.
(18) Wen, C. J.; Huggins, R. A. Chemical Diffusion in Intermediate Phases in the Lithium-Silicon System. *J. Solid State Chem.* **1981**, *37*, 271−278.
(19) Hamzelui, N.; Eshetu, G. G.; Figgemeier, E. Customizing Active Materials and Polymeric Binders: Stern Requirements to Realize Silicon-Graphite Anode Based Lithium-Ion Batteries. *J. Energy Storage* **2021**, *35*, 102098.
(20) Eshetu, G. G.; Figgemeier, E. Confronting the Challenges of Next-Generation Silicon Anode-Based Lithium-Ion Batteries: Role of Designer Electrolyte Additives and Polymeric Binders. *ChemSusChem* **2019**, *12*, 2515−2539.
(21) Bresser, D.; Buchholz, D.; Moretti, A.; Varzi, A.; Passerini, S. Alternative Binders for Sustainable Electrochemical Energy Storage − the Transition to Aqueous Electrode Processing and Bio-Derived Polymers. *Energy Environ. Sci.* **2018**, *11*, 3096−3127.
(22) Kwon, T.-w.; Choi, J. W.; Coskun, A. The Emerging Era of Supramolecular Polymeric Binders in Silicon Anodes. *Chem. Soc. Rev.* **2018**, *47*, 2145−2164.
(23) Eshetu, G. G.; Zhang, H.; Judez, X.; Adenusi, H.; Armand, M.; Passerini, S.; Figgemeier, E. Production of High-Energy Li-Ion Batteries Comprising Silicon-Containing Anodes and Insertion-Type Cathodes. *Nat. Commun.* **2021**, *12*, 5459.
(24) Chae, S.; Choi, S. H.; Kim, N.; Sung, J.; Cho, J. Integration of Graphite and Silicon Anodes for the Commercialization of High-Energy Lithium-Ion Batteries. *Angew. Chem., Int. Ed.* **2020**, *59*, 110.
(25) Aupperle, F.; Eshetu, G. G.; Eberman, K. W.; Xioa, A.; Bridel, J.-S.; Figgemeier, E. Realizing a High-Performance LiNi 0.6 Mn 0.2 Co 0.2 O 2 /Silicon−Graphite Full Lithium Ion Battery Cell via a Designer Electrolyte Additive. *J. Mater. Chem. A* **2020**, *8*, 19573−19587.
(26) Rong, Y.; Hu, Y.; Mei, A.; Tan, H.; Saidaminov, M. I.; Seok, S. I.; McGehee, M. D.; Sargent, E. H.; Han, H. Challenges for Commercializing Perovskite Solar Cells. *Science* **2018**, *361*, No. eaat8235.
(27) Jena, A. K.; Kulkarni, A.; Miyasaka, T. Halide Perovskite Photovoltaics: Background, Status, and Future Prospects. *Chem. Rev.* **2019**, *119*, 3036−3103.
(28) Liu, X.-K.; Xu, W.; Bai, S.; Jin, Y.; Wang, J.; Friend, R. H.; Gao, F. Metal Halide Perovskites for Light-Emitting Diodes. *Nat. Mater.* **2021**, *20*, 10−21.
(29) Cahen, D.; Kronik, L.; Hodes, G. Are Defects in Lead-Halide Perovskites Healed, Tolerated, or Both? *ACS Energy Lett.* **2021**, *6*, 4108−4114.
(30) Siekmann, J.; Ravishankar, S.; Kirchartz, T. Apparent Defect Densities in Halide Perovskite Thin Films and Single Crystals. *ACS Energy Lett.* **2021**, *6*, 3244−3251.
(31) Krückemeier, L.; Krogmeier, B.; Liu, Z.; Rau, U.; Kirchartz, T. Understanding Transient Photoluminescence in Halide Perovskite Layer Stacks and Solar Cells. *Adv. Energy Mater.* **2021**, *11*, 2003489.
(32) Kirchartz, T.; Márquez, J. A.; Stolterfoht, M.; Unold, T. Photoluminescence-Based Characterization of Halide Perovskites for Photovoltaics. *Adv. Energy Mater.* **2020**, *10*, 1904134.
(33) De Wolf, S.; Holovsky, J.; Moon, S.-J.; Löper, P.; Niesen, B.; Ledinsky, M.; Haug, F.-J.; Yum, J.-H.; Ballif, C. Organometallic Halide Perovskites: Sharp Optical Absorption Edge and Its Relation to Photovoltaic Performance. *J. Phys. Chem. Lett.* **2014**, *5*, 1035−1039.
(34) Almora, O.; Baran, D.; Bazan, G. C.; Berger, C.; Cabrera, C. I.; Catchpole, K. R.; Erten-Ela, S.; Guo, F.; Hauch, J.; Ho-Baillie, A. W. Y.; Jacobsson, T. J.; Janssen, R. A. J.; Kirchartz, T.; Kopidakis, N.; Li, Y.; Loi, M. A.; Lunt, R. R.; Mathew, X.; McGehee, M. D.; Min, J.; Mitzi, D. B.; Nazeeruddin, M. K.; Nelson, J.; Nogueira, A. F.; Paetzold, U. W.; Park, N. G.; Rand, B. P.; Rau, U.; Snaith, H. J.; Unger, E.; Vaillant-Roca, L.; Yip, H. L.; Brabec, C. J. Device Performance of Emerging Photovoltaic Materials (Version 2). *Adv. Energy Mater.* **2021**, *11*, 2102526.

https://doi.org/10.1021/acsomega.2c02940
ACS Omega 2022, 7, 27532−27541

(35) Unger, E. L.; Kegelmann, L.; Suchan, K.; Sörell, D.; Korte, L.; Albrecht, S. Roadmap and Roadblocks for the Band Gap Tunability of Metal Halide Perovskites. *J. Mater. Chem. A* **2017**, *5*, 11401−11409.
(36) Jeong, J.; Kim, M.; Seo, J.; Lu, H.; Ahlawat, P.; Mishra, A.; Yang, Y.; Hope, M. A.; Eickemeyer, F. T.; Kim, M.; Yoon, Y. J.; Choi, I. W.; Darwich, B. P.; Choi, S. J.; Jo, Y.; Lee, J. H.; Walker, B.; Zakeeruddin, S. M.; Emsley, L.; Rothlisberger, U.; Hagfeldt, A.; Kim, D. S.; Grätzel, M.; Kim, J. Y. Pseudo-Halide Anion Engineering for α-FAPbI3 Perovskite Solar Cells. *Nature* **2021**, *592*, 381−385.
(37) Yoo, J. J.; Seo, G.; Chua, M. R.; Park, T. G.; Lu, Y.; Rotermund, F.; Kim, Y.-K.; Moon, C. S.; Jeon, N. J.; Correa-Baena, J.-P.; Bulović, V.; Shin, S. S.; Bawendi, M. G.; Seo, J. Efficient Perovskite Solar Cells via Improved Carrier Management. *Nature* **2021**, *590*, 587−593.
(38) Yim, T.; Choi, S. J.; Jo, Y. N.; Kim, T.-H.; Kim, K. J.; Jeong, G.; Kim, Y.-J. Effect of Binder Properties on Electrochemical Performance for Silicon-Graphite Anode: Method and Application of Binder Screening. *Electrochim. Acta* **2014**, *136*, 112−120.
(39) Koo, B.; Cho, J.; Choi, N.-S.; Cho, Y.; Kim, H.; Lee, K. T. A Highly Cross-Linked Polymeric Binder for High-Performance Silicon Negative Electrodes in Lithium Ion Batteries. *Angew. Chem., Int. Ed.* **2012**, *51*, 8762−8767.
(40) Preman, A. N.; Lee, H.; Yoo, J.; Kim, I. T.; Saito, T.; Ahn, S.-k. Progress of 3D Network Binders in Silicon Anodes for Lithium Ion Batteries. *J. Mater. Chem. A* **2020**, *8*, 25548−25570.
(41) Aupperle, F.; von Aspern, N.; Berghus, D.; Weber, F.; Eshetu, G. G.; Winter, M.; Figgemeier, E. The Role of Electrolyte Additives on the Interfacial Chemistry and Thermal Reactivity of Si-Anode-Based Li-Ion Battery. *ACS Appl. Energy Mater.* **2019**, *2*, 6513−6527.
(42) Liu, Z.; Krückemeier, L.; Krogmeier, B.; Klingebiel, B.; Márquez, J. A.; Levcenko, S.; Öz, S.; Mathur, S.; Rau, U.; Unold, T.; Kirchartz, T. Open-Circuit Voltages Exceeding 1.26 v in Planar Methylammonium Lead Iodide Perovskite Solar Cells. *ACS Energy Lett.* **2019**, *4*, 110−117.
(43) Haddad, J.; Krogmeier, B.; Klingebiel, B.; Krückemeier, L.; Melhem, S.; Liu, Z.; Hüpkes, J.; Mathur, S.; Kirchartz, T. Analyzing Interface Recombination in Lead-Halide Perovskite Solar Cells with Organic and Inorganic Hole-Transport Layers. *Adv. Mater. Interfaces* **2020**, *7*, 2000366.
(44) Krückemeier, L.; Liu, Z.; Krogmeier, B.; Rau, U.; Kirchartz, T. Consistent Interpretation of Electrical and Optical Transients in Halide Perovskite Layers and Solar Cells. *Adv. Energy Mater.* **2021**, *11*, 2102290.
(45) Chen, Z.; Zhang, L.; Wu, X.; Song, K.; Ren, B.; Li, T.; Zhang, S. Effect of N/P Ratios on the Performance of LiNi0.8Co0.15Al0.05O2|| SiOx/Graphite Lithium-Ion Batteries. *J. Power Sources* **2019**, *439*, 227056.
(46) Kim, C.-S.; Jeong, K. M.; Kim, K.; Yi, C.-W. Effects of Capacity Ratios between Anode and Cathode on Electrochemical Properties for Lithium Polymer Batteries. *Electrochim. Acta* **2015**, *155*, 431−436.
(47) Kasavajjula, U.; Wang, C.; Appleby, A. J. Nano- and Bulk-Silicon-Based Insertion Anodes for Lithium-Ion Secondary Cells. *J. Power Sources* **2007**, *163*, 1003−1039.
(48) Kasnatscheew, J.; Placke, T.; Streipert, B.; Rothermel, S.; Wagner, R.; Meister, P.; Laskovic, I. C.; Winter, M. A Tutorial into Practical Capacity and Mass Balancing of Lithium Ion Batteries. *J. Electrochem. Soc.* **2017**, *164*, A2479−A2486.
(49) Piernas-Muñoz, M. J.; Trask, S. E.; Dunlop, A. R.; Lee, E.; Bloom, I. Effect of Temperature on Silicon-Based Anodes for Lithium-Ion Batteries. *J. Power Sources* **2019**, *441*, 227080.
(50) Wang, Q.; Sun, J.; Yao, X.; Chen, C. Thermal Stability of LiPF6/EC + DEC Electrolyte with Charged Electrodes for Lithium Ion Batteries. *Thermochim. Acta* **2005**, *437*, 12−16.
(51) Choi, N.-S.; Han, J.-G.; Ha, S.-Y.; Park, I.; Back, C.-K. Recent Advances in the Electrolytes for Interfacial Stability of High-Voltage Cathodes in Lithium-Ion Batteries. *RSC Adv.* **2015**, *5*, 2732−2748.
(52) Jung, R.; Strobl, P.; Maglia, F.; Stinner, C.; Gasteiger, H. A. Temperature Dependence of Oxygen Release from LiNi 0.6 Mn 0.2 Co 0.2 O 2 (NMC622) Cathode Materials for Li-Ion Batteries. *J. Electrochem. Soc.* **2018**, *165*, A2869−A2879.
(53) Rodrigues, M.-T. F.; Babu, G.; Gullapalli, H.; Kalaga, K.; Sayed, F. N.; Kato, K.; Joyner, J.; Ajayan, P. M. A Materials Perspective on Li-Ion Batteries at Extreme Temperatures. *Nat. Energy* **2017**, *2*, 17108.
(54) Jiang, J.-A.; Su, Y.-L.; Kuo, K.-C.; Wang, C.-H.; Liao, M.-S.; Wang, J.-C.; Huang, C.-K.; Chou, C.-Y.; Lee, C.-H.; Shieh, J.-C. On a Hybrid MPPT Control Scheme to Improve Energy Harvesting Performance of Traditional Two-Stage Inverters Used in Photovoltaic Systems. *Renew. Sustain. Energy Rev.* **2017**, *69*, 1113−1128.
(55) Belhachat, F.; Larbes, C. A Review of Global Maximum Power Point Tracking Techniques of Photovoltaic System under Partial Shading Conditions. *Renew. Sustain. Energy Rev.* **2018**, *92*, 513−553.

https://doi.org/10.1021/acsomega.2c02940
ACS Omega 2022, 7, 27532−27541